

# UC Santa Barbara

## UC Santa Barbara Previously Published Works

### Title

Selective undercut etching of InGaAs and InGaAsP quantum wells for improved performance of long-wavelength optoelectronic devices

### Permalink

<https://escholarship.org/uc/item/1443w8vg>

### Journal

Journal of Lightwave Technology, 24(3)

### ISSN

0733-8724

### Authors

Pasquariello, D  
Bjorlin, E S  
Lasaosa, D  
[et al.](#)

### Publication Date

2006-03-01

Peer reviewed

# Selective Undercut Etching of InGaAs and InGaAsP Quantum Wells for Improved Performance of Long-Wavelength Optoelectronic Devices

Donato Pasquariello, E. Staffan Björilin, *Member, IEEE*, Daniel Lasasosa, Yi.-Jen Chiu, Joachim Piprek, *Senior Member, IEEE*, and John E. Bowers, *Fellow, IEEE*

**Abstract**—In this paper, the authors show how selective undercut etching of InGaAs- and InGaAsP-based quantum wells (QWs) can improve the performance of InP-based optoelectronic devices. First, wet-chemical-etching characteristics are investigated. Mixtures of sulphuric and hydrogen peroxide acids are used as wet-etching solutions, and properties such as etch rates, selectivity, and anisotropy are studied in detail. Problems arising from the anisotropic nature of the etching are analyzed, and their impact on device design and performance is discussed. Second, the authors present several optoelectronic devices where selective undercut etching of InGaAs- or InGaAsP-based multiquantum wells (MQWs) improves device performance; these devices include electroabsorption modulators (EAMs), vertical-cavity semiconductor optical amplifiers (VCSOAs), and waveguide amplifier photodetectors (WAPs). Very high extinction ratios were obtained for the EAM. A selective undercut-etched VCSOA reached a record-high 17-dB fiber-to-fiber gain, and the WAP demonstrated an external quantum efficiency higher than 100%.

**Index Terms**—Electroabsorption modulator (EAM), photodiode, semiconductor optical amplifier (SOA), undercut etching.

## I. INTRODUCTION

WET CHEMICAL etching of InP and lattice-matched materials plays an essential role in the fabrication of microelectronic and optoelectronic devices such as heterojunction bipolar transistors (HBTs), lasers, modulators, and photodetectors. As performance of microelectronic and optoelectronic devices is pushed to the limit, a higher accuracy and control is required in the fabrication and etching steps. For InP and most lattice-matched materials, several wet-etching solutions are available. Extensive reviews of wet chemical etching of III–V materials, in general, and InP/InGaAsP materials, in particular, are found in [1]–[3]. Wet etching of InGaAs and InGaAsP using  $\text{H}_2\text{SO}_4 : \text{H}_2\text{O}_2 : \text{H}_2\text{O}$  solutions has been previously described in [4]–[7]. These solutions are routinely used for fabricating InP-based optoelectronic devices, e.g., for patterning and etching through InGaAsP quantum wells (QWs). However, detailed information about the etching characteristics, such as etch rates, selectivity and anisotropy, are still unavailable in literature. Therefore, in this paper, we present a detailed study of selective

undercut etching of InGaAs- and InGaAsP-based multiquantum wells (MQWs) using  $\text{H}_2\text{SO}_4 : \text{H}_2\text{O}_2 : \text{H}_2\text{O}$  solutions.

Several optoelectronic devices are presented where undercut etching the InGaAsP-based MQW improves the device performance. It is shown that selective undercut etching the MQWs in vertical-cavity semiconductor optical amplifiers (VCSOAs) [8] and waveguide amplifier photodetectors (WAPs) [9] results in improved carrier and current confinement, respectively. In electroabsorption modulators (EAMs), selectively etching the MQW region can reduce the junction capacitance and scattering losses of the waveguide and improve the mode profile.

## II. SELECTIVE UNDERCUT ETCHING

### A. Experiment and Results

For the undercut-etching experiments, undoped lattice-matched  $\text{In}_{0.53}\text{Ga}_{0.47}\text{As}$  layers and undoped InGaAsP MQWs were grown by metal–organic chemical vapor deposition (MOCVD) on (100) oriented n-type InP wafers. The InGaAsP MQW consisted of six compressively strained  $\text{In}_{0.76}\text{Ga}_{0.24}\text{As}_{0.79}\text{P}_{0.21}$  QWs and  $\text{In}_{0.71}\text{Ga}_{0.29}\text{As}_{0.55}\text{P}_{0.45}$  barriers for a peak emission at 1550 nm [10]. The InGaAs layer and the InGaAsP MQW were embedded between InP cladding layers. An  $\text{SiN}_x$  mask and  $\text{CH}_4 : \text{H}_2 : \text{Ar}$  dry etching was used to pattern mesa stripes in the  $\langle 011 \rangle$  and  $\langle 010 \rangle$  directions. The  $\langle 011 \rangle$  directions are cleaving directions for InP wafers and the directions in which most in-plane devices are aligned. The  $\langle 010 \rangle$  directions lie  $45^\circ$  from the  $\langle 011 \rangle$  direction on a (100) wafer. The mesas were selectively undercut etched using  $\text{H}_2\text{SO}_4 : \text{H}_2\text{O}_2 : \text{H}_2\text{O} = 3 : 1 : 1$  and  $\text{H}_2\text{SO}_4 : \text{H}_2\text{O}_2 : \text{H}_2\text{O} = 1 : 1 : 10$  solutions. All etchings were done at room temperatures. The mesa stripes were then cleaved, and the undercut depth was measured using an SEM.

The undercut etching of InGaAs was measured in a ( $\text{H}_2\text{SO}_4 : \text{H}_2\text{O}_2 : \text{H}_2\text{O} = 3 : 1 : 1$ ) solution. InGaAs etches very fast in this concentrated solution, with an etch rate of  $3 \mu\text{m}/\text{min}$  and  $10 \mu\text{m}/\text{min}$  in the  $\langle 011 \rangle$  and  $\langle 001 \rangle$  directions, respectively. The rate of undercut etching of an InGaAsP MQW in the ( $\text{H}_2\text{SO}_4 : \text{H}_2\text{O}_2 : \text{H}_2\text{O} = 3 : 1 : 1$ ) solution was also measured. Etch rates of  $0.6 \mu\text{m}/\text{min}$  in the  $\langle 011 \rangle$  directions and  $1.15 \mu\text{m}/\text{min}$  in the  $\langle 001 \rangle$  directions were obtained. The etch rate of InGaAsP is lower than that of InGaAs as could be expected for  $\text{H}_2\text{SO}_4 : \text{H}_2\text{O}_2 : \text{H}_2\text{O}$  solutions. In these solutions, the higher the P-content of the layer, the lower the etch rate. For comparison,

Manuscript received October 11, 2004; revised October 24, 2005.

The authors are with the Department of Electrical and Computer Engineering, University of California, Santa Barbara, CA 93106 USA (e-mail: bowers@ece.ucsb.edu).

Digital Object Identifier 10.1109/JLT.2005.863227

TABLE I  
SUMMARY OF ETCH RESULTS

<i>Material/Direction:</i>	<i>Etch-rate (<math>\mu\text{m}/\text{min}</math>) in 3:1:1</i>	<i>Etch-rate (<math>\mu\text{m}/\text{min}</math>) in 1:1:10</i>
InGaAs/[011]	$3 \pm 0.4$	$0.22 \pm 0.004$
InGaAs/[001]	$10 \pm 2.1$	—
InGaAsP MQW/[011]	$0.6 \pm 0.05$	$0.08 \pm 0.005$
InGaAsP MQW/[001]	$1.15 \pm 0.05$	—
InP	$6.3 \cdot 10^{-3} \pm 1.5 \cdot 10^{-4}$	$2.6 \cdot 10^{-3} \pm 1 \cdot 10^{-4}$
<i>Selectivity:</i>		
InGaAs [011]/InP	476.2	84.6
InGaAs [001]/InP	1578.3	—
InGaAsP MQW [011]/InP	95.2	30.8
InGaAsP MQW [001]/InP	182.5	—

the etch rates of InGaAs and InGaAsP MQWs were measured in a more diluted solution ( $\text{H}_2\text{SO}_4 : \text{H}_2\text{O}_2 : \text{H}_2\text{O} = 1 : 1 : 10$ ). The etch rate decreases drastically to  $0.22 \mu\text{m}/\text{min}$  for InGaAs and to  $0.08 \mu\text{m}/\text{min}$  for InGaAsP MQWs in the  $\langle 011 \rangle$ -directions. The slow etch rate results in long etching times; therefore, the etch selectivity to InP should be addressed. Most cladding layers are composed of InP in long-wavelength optoelectronic devices. The InP etch rate was measured in 3:1:1 and 1:1:10 solutions. The InP etch rates in 3:1:1 and 1:1:10 solutions were  $1.05$  and  $0.44 \text{ \AA}/\text{s}$ , respectively. Table I summarizes these etch results. The 3:1:1 solution is more selective than the 1:1:10 solution and may, therefore, be the best choice even if it etches InP at a faster rate.

For both InGaAs and InGaAsP MQWs, the etch rate was the same in all  $\langle 001 \rangle$  directions and in all  $\langle 011 \rangle$  directions ( $\langle 001 \rangle$  is the full set of equivalent [001], [010], [100] directions;  $\langle 011 \rangle$  is the full set of equivalent [011], [110], [101] directions). For InGaAs, the only difference in the undercut characteristics between orthogonal directions, i.e., [011] and [0-11], was the slope of the sidewalls forming an angle of  $55^\circ$  and  $125^\circ$ , respectively, with the substrate. Undercut etching the InGaAsP-based MQW resulted in a tapered-shape sidewall profile. This was also reported in undercut-etched vertical-cavity surface emitting lasers (VCSELs) [11]. The tapered undercut etching is probably due to compositional difference between barriers, wells, and the separate-confinement heterostructure (SCH) layers.

Previously, it was seen that there is an apparent difference in the etch rates between the  $\langle 011 \rangle$  and the  $\langle 001 \rangle$  directions. The undercut etch rates of InGaAs and InGaAsP MQWs were considerably faster in the  $\langle 001 \rangle$  directions than in the  $\langle 011 \rangle$  directions. Fig. 1 shows the anisotropy when selectively undercut etching InGaAs. For the circular mesa in Fig. 1(a), the undercut has a rectangular structure. This is because the undercut etching is faster in the  $\langle 001 \rangle$  directions. Fig. 1(b) shows rectangular mesas with sides oriented along the  $\langle 011 \rangle$  direction. For these structures, the undercut etching is faster at the corners than along the sides. Fig. 1(c) shows the undercut etching of rectangular mesas oriented along the  $\langle 001 \rangle$  direction. For these mesas, the anisotropy is not seen because the sides are

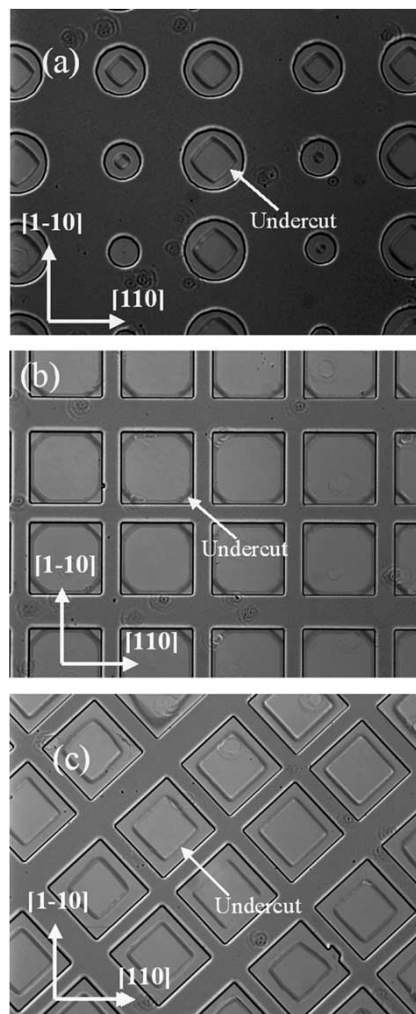


Fig. 1. Undercut-etched structures. (a) Circular-shaped mesa, (b) rectangular-shaped mesa with sides oriented along the  $\langle 110 \rangle$  directions, and (c) rectangular-shaped mesa with sides oriented along the  $\langle 001 \rangle$  directions.

oriented along the fast-etching  $\langle 001 \rangle$  directions. Fig. 2 shows an “etch rose” [12]. It consists of circle sectors with an angular resolution of  $1^\circ$ . Fig. 2(b) show a schematic picture of the mask used for each circle sector. Through  $360^\circ$ , each sector represents a different plane along the radial face. Each circle sector yields the undercut etch rate in the tangential direction. The length of an undercut circle sector decreases as the undercutting increases, which forms the “rose pattern.” From the etch rose, it is obvious that the fastest etch rate is in the  $\langle 001 \rangle$  directions and the slowest etch rate is in the  $\langle 011 \rangle$  directions; the etch rates in all other directions lie in between these two extremes.

### B. Crystallographic Aspects

III-V semiconductors have two types of  $\{111\}$  surfaces: the III $\{111\}$  and the V $\{111\}$  surfaces. The outermost atom layer on III $\{111\}$  and V $\{111\}$  surfaces consist of group-III atoms and group-V atoms, respectively, that have three covalent bondings with the crystal lattice. Group-III surface atoms have three bonding electrons per atom that are all bonded to the lattice. Group-V surface atoms have five bonding electrons per

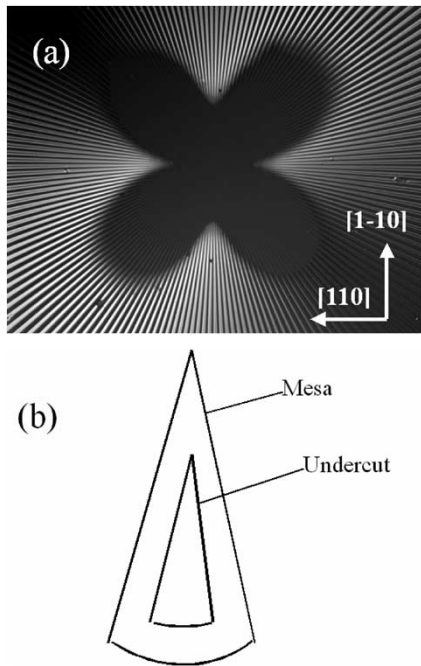


Fig. 2. (a) "Etch rose" showing the undercut anisotropy on a (100) surface. (b) One sector of the "etch rose" mask. The undercut in the radial face decrease the length of the sector.

atom; therefore, two of these are "dangling" electrons.  $V\{111\}$  surfaces are therefore more reactive than  $III\{111\}$  surfaces and should have higher etch rates.  $III\{111\}$  are also referred to as  $\{111\}A$  planes, and  $V\{111\}$  are also referred to as  $\{111\}B$  planes. The etch rate in a crystallographic direction is determined by the relative orientation to the slow-etching  $\{111\}A$  planes. The sidewall angles in undercut etching InGaAs clearly matches with theoretical  $54^\circ 44'$  and  $125^\circ 16'$  angles that the  $\{111\}A$  planes form with the (001) surface on (0-11) and (011) cleavage planes. The etching proceeds up to the  $\{111\}A$  planes, which are the slow-etching planes that determine the etch rate. Undercut etching in the  $\langle 001 \rangle$  direction proceeds at a faster rate because there are no  $\{111\}A$  planes that slow down the etching. For undercut etching in the  $\langle 011 \rangle$  directions, the relative orientation to the  $\{111\}A$  planes slows down the etch rate. The etch rose in Fig. 2 visualizes the undercut-etch anisotropy in InGaAs. The undercut-etching rate in a specific crystallographic direction is in between the fast etching  $\langle 001 \rangle$  directions and the slow etching  $\langle 011 \rangle$  directions. Fig. 3 shows the relative orientation of the polar  $\{111\}A$  and  $\{111\}B$  planes on a (001) wafer. It is worth noting that, in many semiconductors, the etch rate of  $\{111\}$  planes can be so slow that it acts as an efficient "etch stop."

### III. DEVICES

#### A. Electroabsorption Modulator (EAM)

One major advantage of using III-V in-plane waveguide-type modulators is that they can be monolithically integrated with lasers and the driving circuitry. Two common types of in-plane modulators are EAMs and electrooptical modulators (EOMs). EAMs normally have a lower drive voltage and a higher extinc-

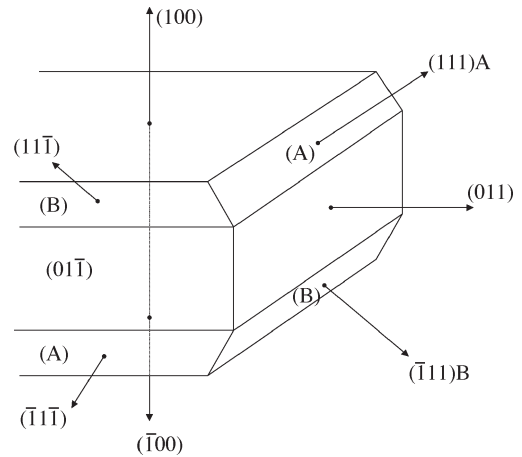


Fig. 3. Relative crystallographic location of  $\{111\}A$  and  $\{111\}B$  planes.

tion ratio than EOMs, such as Mach-Zehnder interferometer modulators. In-plane EAMs use either the Franz-Keldysh effect (bulk active region) or the quantum-confined Stark effect (MQW active region) to go from, ideally, a passive to an absorbing waveguide. The advantage of using EAMs based on the quantum-confined Stark effect is that absorption edge is much sharper and moves faster with the applied electrical field, yielding a lower drive voltage and a higher extinction ratio. The disadvantage consequently being the higher temperature and wavelength sensitivity as compared to Franz-Keldysh EAMs.

A long EAM device has the advantage of a reduced drive voltage and an increased extinction ratio. Unfortunately, increasing the device length also results in a reduced bandwidth. Decreasing the junction capacitance and thereby improving the modulation speed can be done in two ways: either by making the intrinsic region thicker or by reducing the width of the waveguide. Increasing the intrinsic region thickness will increase the drive voltage, while reducing the waveguide width may be difficult due to the increased fabrication complexity. With a narrow EAM waveguide, optical scattering losses are also likely to increase. As suggested by Zhang [13], an alternative way to improve the bandwidth is to selectively undercut etch the intrinsic region. This reduces the capacitance without increasing optical scattering losses. The optical mode will be confined by the undercut etching, reducing the optical scattering losses at the sidewalls. Also, by undercutting the waveguide, the top p-InP cladding layer can be wider than the active region thereby avoiding an increase in resistance from the cladding layers and from the metal-semiconductor contact, which would otherwise result in an increased microwave loss. Increased contact resistance and cladding-layer resistance are inevitable if a reduction of the junction capacitance is realized by reducing the width of the waveguide. The maximum undercut-etch depth of the EAM waveguide is limited by the increased optical coupling and insertion losses.

Fig. 4 shows an SEM cross section of an in-plane traveling-wave EAM, where the InGaAsP-based MQW region has been selectively undercut etched. Very high extinction ratios were obtained. Fig. 5 shows the fiber-to-fiber transmission versus the reverse bias for the TM and TE modes in an undercut EAM. Extinction ratios of 10 and 20 dB were obtained for the TE mode

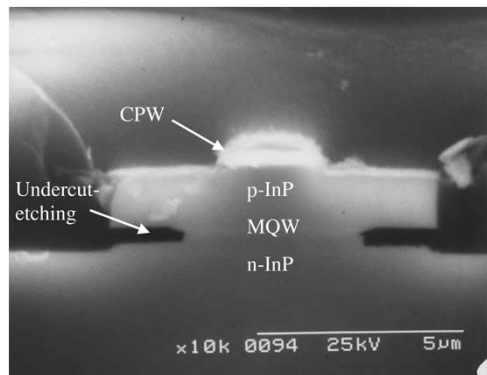


Fig. 4. SEM cross section of a traveling-wave EAM with an undercut-etched active region.

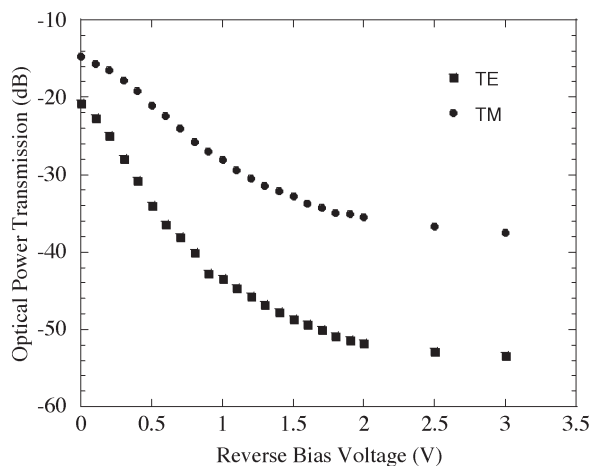


Fig. 5. Fiber-to-fiber transmission for an EAM at 1550 nm.

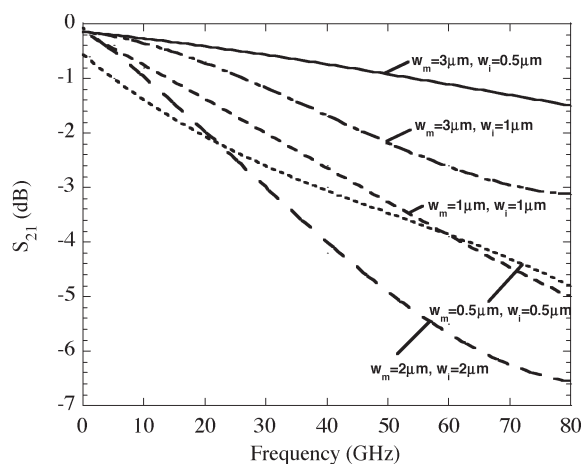


Fig. 6. Calculated electrical-to-electrical  $S_{21}$  response for an EAM with and without undercut etching.

at 0.4 and 0.8 V, respectively. Extinction ratios of 10 and 20 dB were obtained for the TM mode at 0.8 and 1.7 V, respectively. The deposition of an antireflection coating on the cleaved waveguide facets will further reduce coupling and insertion losses in the EAM. Fig. 6 shows the calculated  $S_{21}$  response for a 300- $\mu$ m long EAM waveguide, with and without undercut etching. The ridge width at the top cladding ( $w_m$ ) and intrinsic region width ( $w_i$ ) are varied to simulate EAMs with and

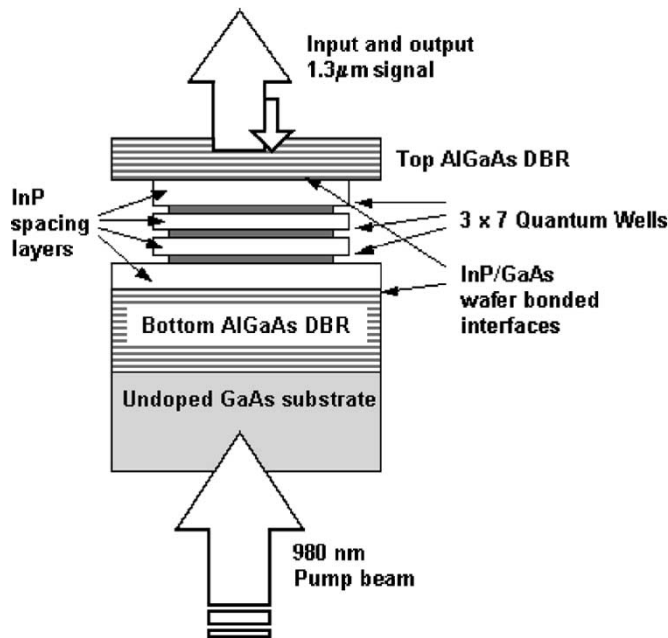


Fig. 7. Schematic picture of a VCISOA operating in the reflection mode. The three gain regions and the respective QWs are undercut etched.

without undercut etching. The electrical-to-electrical response of the EAM is normally described by the  $S$  parameters.  $S_{21}$  is the transmission coefficient through the EAM and includes both the microwave propagation loss and the impedance mismatch (a 50- $\Omega$  input is assumed). The  $S_{21}$  parameter was calculated from equations found in [14]. Reducing the ridge width from 2 to 0.5  $\mu$ m definitely improves the bandwidth; however, at a certain point, the increased resistance at the top cladding layer limits the bandwidth. In Fig. 6, the highest bandwidth is obtained for EAMs with large ridge widths ( $w_m$ ) and narrow active-region width ( $w_i$ ). A wide ridge reduces both the top p-InP cladding resistance and the metal contact resistance, while a narrow active region reduces the junction capacitance per unit length.

**B. Vertical-Cavity Semiconductor Optical Amplifier (VCISOA)**

Optical amplifiers are used for a wide variety of applications in optical communication systems. The three most basic functions are booster amplifiers, in-line amplifiers, and preamplifiers. Previously, semiconductor optical amplifiers (SOAs) were considered as the most promising candidates. This changed with the introduction of erbium-doped fiber amplifiers (EDFAs), which at present date have little competition in terms of performance. However, currently, there is an increasing interest in low-cost alternatives for access networks. VCISOAs are a new class of devices developed for such applications [8]. VCISOAs have several advantages over in-plane SOAs, such as high coupling efficiency, polarization-independent gain, and low power consumption because of a smaller active region. In addition, the vertical-cavity design allows on-wafer testing and fabrication of two-dimensional arrays. Fig. 7 shows a schematic sketch of a VCISOA operating in the reflection mode. The structure consists of a stacked InGaAsP-based MQW active-region wafer bonded between two AlGaAs/GaAs distributed Bragg

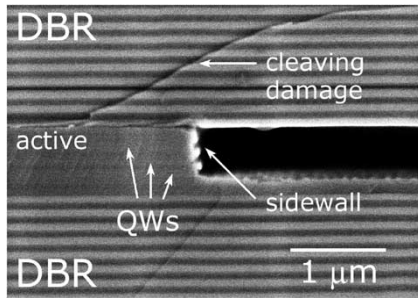


Fig. 8. SEM cross section of a VCSEA. The undercut-etched QWs sidewalls are covered with InP from the mass transport.

reflectors (DBRs). The InGaAsP-based active region consists of three gain regions with seven compressively strained wells and strain compensating barriers in each. InP spacer layers separate the three gain regions. Details of the device structure and the fabrication process can be found in [8].

The VCSEAs used in this study were optically pumped and operated in the reflection mode. A 980-nm laser diode was used as the pump source, and a tuneable 1300-nm external cavity laser diode was used as signal source. The  $1/e^2$  diameters of the input signal and the pump beam was measured to 8.3 and 8.8  $\mu\text{m}$ , respectively.

A large improvement in efficiency and gain can be obtained by confining the carriers, which is achieved by confining the lateral dimensions of the active region. The devices show higher quantum efficiency because the carriers cannot diffuse laterally in the QWs; therefore, the carrier density in the active region is increased. The lateral confinement was obtained by patterning and dry etching the InGaAsP-based MQW active region into circular mesas before wafer bonding the Bragg mirrors. The carrier confinement depends both on the dimensions of the mesa and on the properties of the sidewalls. A large recombination current can occur at the sidewalls if they are not properly passivated. For these VCSEAs, the sidewall passivation was obtained by selective undercut etching the InGaAsP-based QWs and barriers using a  $\text{H}_2\text{SO}_4 : \text{H}_2\text{O}_2 : \text{H}_2\text{O}$  solution. It is likely that the mass transport of InP from the cladding and spacer layers, during the bonding of the last AlGaAs/GaAs Bragg mirror to the active region (performed at 575  $^\circ\text{C}$ ), fills the selectively undercut-etched steps at the sidewalls. The surface recombination of carriers is certainly reduced by covering the sidewalls of the patterned InGaAsP-based active region with a wider-bandgap material, like InP [15], [16]. Fig. 8 shows an SEM cross section where the three gain regions (InGaAsP-based MQWs) have been selectively under-etched, leaving the InP spacer layer clearly visible. The initially steplike profile of the sidewall is smoothed due to surface migration and mass transport of InP to the under-etched steps, cf. Fig. 7. However, further investigations are required to establish the exact composition and crystalline structure of the material covering the QW sidewalls. It is probable that the surface recombination at the sidewalls of the active region was suppressed by the selective undercut etching of InGaAsP QWs and the subsequent mass transport of InP filling these steps. A similar procedure was previously shown for buried heterostructure lasers [17]. In addition to the lateral carrier confinement obtained by pat-

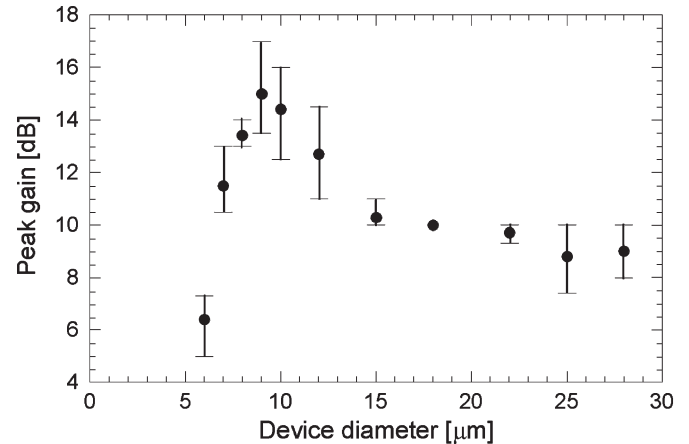


Fig. 9. Peak gain in a VCSEA as a function of the active-region diameter.

tern the InGaAsP-based active region into circular mesas, the gain and the efficiency of the VCSEAs were further improved by suppressing the surface recombination at the sidewalls of the active region.

VCSEAs with patterned active regions with diameters ranging from 5 to 36  $\mu\text{m}$  were fabricated. Fig. 9 shows the peak fiber-to-fiber gain as a function of the device diameter. The dots are average values for at least three devices, and the error bars represent extreme values. For active regions with diameters larger than 15  $\mu\text{m}$ , the gain is size independent. In this case, the active region is wider than the pump-beam diameter of 8.8  $\mu\text{m}$ . The carriers recombine before they reach the sidewalls of the active region, and the lateral carrier confinement has no effect. The diffusion length in strained InGaAsP QWs is in the order of 1–2  $\mu\text{m}$  [15]. The carrier confinement results in an increased peak gain only for active-region diameters smaller than about 15  $\mu\text{m}$ . The smaller the active region, the higher the carrier density becomes. The highest fiber-to-fiber peak gain of 17 dB was obtained for active-region diameters of 9  $\mu\text{m}$ . When the size of the active-region diameter decreases further and approaches the signal spot size (8.3  $\mu\text{m}$ ) the peak gain decreases due to the increased optical scattering loss at sidewalls (the active region was patterned through dry etching, which increases the sidewall roughness). For active-region diameters smaller than the signal and pump-beam spot size, the gain drops dramatically as expected.

### C. Waveguide Amplifier Photodetector (WAP)

In an externally modulated analog fiberoptic link, high-speed and high-efficiency photodetectors with high saturation power can improve the overall link performance parameters, such as link gain, noise figure, and spurious free dynamic range (SFDR) [18]. For these applications, there is an increasing interest in waveguide photodetectors, which are often referred to as edge-coupled photodetectors. Using waveguide photodetectors, the inherent tradeoff between efficiency and bandwidth that is present in conventional surface-illuminated photodetectors is circumvented [19]. A drawback in using waveguide photodetectors is the increased coupling loss, resulting in a reduced efficiency and an increased noise figure. Pre-amplification of

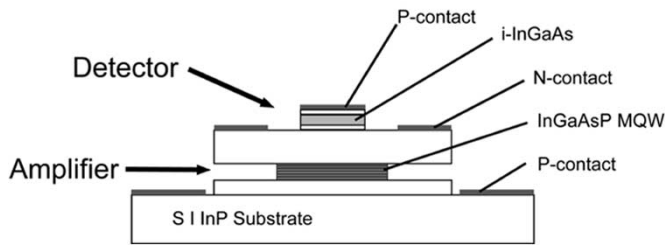


Fig. 10. Schematic cross section of the waveguide amplification photodetector.

the incoming optical power is normally used to improve the efficiency and to boost the output power. However, with preamplification, one faces the possibility of detector saturation and the introduction of the nonlinearity.

Recently, we presented a novel type of monolithic waveguide photodetectors designed to achieve simultaneously high efficiency, high bandwidth, and high saturation power and therefore ideal for use in analog fiber-optic communication systems [20]. WAPs combine optical detection and amplification in a distributed way. The device consists of a p-i-n waveguide photodetector grown on top of an SOA structure. Fig. 10 shows a schematic cross section of a WAP. When the optical power is coupled into the device, a propagating optical mode is generated. The optical mode is simultaneously amplified and absorbed during propagation in the waveguide due to a simultaneous overlap with both the amplifier and the detector region. At the equilibrium between the gain and the absorption, the same number of photons are absorbed in the detector region and brought back to the mode by the amplifier. Thus, ideally, optical power remains constant during propagation in the device. Therefore, the longer the WAP, the higher the efficiency. The interesting characteristic of the WAP is that a very high efficiency is obtained while circumventing detector saturation. Detailed discussions about the performance of WAPs are found in [20].

A 250-nm-thick i-InGaAs layer was used as the absorber, and the optical gain comes from six compressive strained  $\text{In}_{0.76}\text{Ga}_{0.24}\text{As}_{0.79}\text{P}_{0.21}$  QWs separated by strain-compensating  $\text{In}_{0.71}\text{Ga}_{0.29}\text{As}_{0.55}\text{P}_{0.45}$  barriers. A thick n-InP cladding layer separates the absorption and the gain regions. The thickness of the n-InP cladding is important for the WAP performance, because it determines the mode overlap with the amplification and the detection regions of the device. The device has a p-n-p structure. The top p-contact was Ti/Pt/Au, the center n-contact consisted of Ni/AuGe/Ni/Au, and a Pd/Zn/Pd/Au metallization was used for the bottom p-contact.

First, InGaAs in the detector region was undercut etched to reduce the leakage current. A short undercut etching of InGaAs using  $\text{H}_2\text{SO}_4 : \text{H}_2\text{O}_2 : \text{H}_2\text{O}$  is efficient in removing residues from the processing, such as sidewall damage and hydrocarbon contamination, which are known to be a major cause of leakage currents in InGaAs p-i-n detectors [21]. However,  $\text{H}_2\text{SO}_4 : \text{H}_2\text{O}_2 : \text{H}_2\text{O}$  etching leaves a conductive surface oxide on the detector sidewalls. After the undercut etching, a short HF dip removes the conductive surface oxide. Fig. 11 shows detector dark current after each etching step.

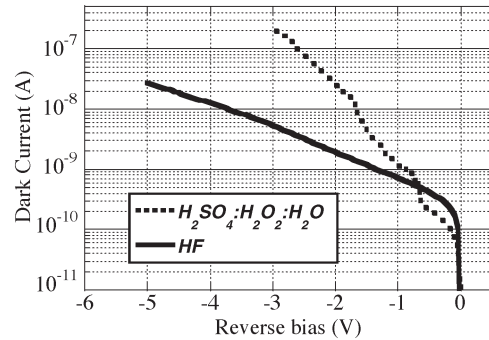


Fig. 11. Detector reverse current after two-step etching. Each curve shows the reverse current after each etching step.

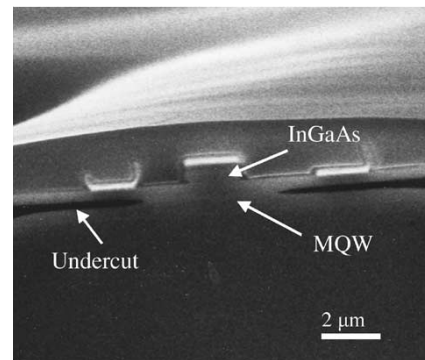


Fig. 12. SEM cross section of a waveguide amplification photodetector. The undercut-etched QWs in the amplifier region is clearly visible.

Using this two-step sidewall etching the detector dark current was effectively reduced. Second, the InGaAsP MQW in the amplifier region was undercut etched. This was necessary to confine the injection current in the amplifier region; otherwise, the sheet resistance of the p-contact layers would result in heavy current crowding. Fig. 12 shows an SEM picture of the cross section of an undercut etched WAP. It is important that the etching solution has a high selectivity to avoid etching the n-InP cladding. Therefore, the  $\text{H}_2\text{SO}_4 : \text{H}_2\text{O}_2 : \text{H}_2\text{O} = 3 : 1 : 1$  solution was used. Another problem with undercut etching the MQW was the bending of released structures. Probably, the thermal mismatch between the n-metal contact and the n-InP layers introduced stress in the released structures. This stress caused the structure to bend heavily and sometimes even break. To compensate for the internal stress in the released structure, a strain-compensating  $\text{SiO}_x/\text{SiN}_y$  stack was deposited by plasma-enhanced chemical vapor deposition (PECVD).  $\text{SiO}_x$  has an internal tensile stress, and  $\text{SiN}_y$  has an internal compressive stress. The purpose the  $\text{SiO}_x/\text{SiN}_y$  layers is twofold: 1) It increases the stiffness of the released structure and 2) by choosing the right thickness of the  $\text{SiO}_x$  film and the  $\text{SiN}_y$  film, the internal strain in the released structure can be compensated.

Fig. 13 shows the photocurrent as a function of the amplifier bias current for a 150- $\mu\text{m}$  long device at 2.2- $\mu\text{W}$  input power. At a low amplifier bias current, there is not much increase in the photocurrent. However, once the amplifier is biased above transparency, the input signal starts experiencing a gain. An external quantum efficiency of 110%, corresponding to

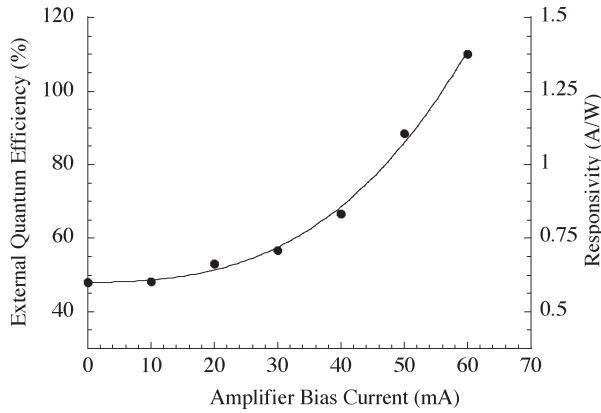


Fig. 13. External quantum efficiency and responsivity as function of amplifier bias current.

a responsivity of 1.375 A/W, was obtained for an amplifier bias current of 60 mA. At higher bias currents, the thermal rollover dominates the amplifier characteristics. The first generation InP-based WAPs thus demonstrate a proof-of-concept. However, WAPs could potentially produce responsivity orders of higher magnitudes [9]. Much of the improvement lies in thermal management and in the optical design of the waveguide to achieve a balance between the gain and the absorption for the propagating optical mode. A photodetector with a very high efficiency and a very high saturation will find a wide range of applications, especially for analog communication links.

#### IV. DISCUSSION AND SUMMARY

We have reviewed undercut-etching characteristics of InGaAs- and InGaAsP-based MQWs in  $\text{H}_2\text{SO}_4 : \text{H}_2\text{O}_2 : \text{H}_2\text{O}$  solutions and, more significantly, shown how these can be used to improve performance of long-wavelength optoelectronic devices.

For EAMs, selective undercut etching of the InGaAsP-based MQW active region can be used to increase the bandwidth. The unit junction capacitance is decreased without increasing the resistance in the top cladding layer and the metal contact. Also, undercut etching the waveguide confines the optical mode, which reduces scattering losses due to sidewall roughness (resulting from RIE). Reducing the scattering losses becomes especially important for very long EAMs. A long EAM has the inherent advantage of yielding a higher extinction ratio and a lower drive voltage.

In VCISOAs, selective undercut etching the InGaAsP MQWs is believed to facilitate the subsequent mass transport of InP to the active region, resulting in efficient sidewall passivation. InP has a larger bandgap than InGaAsP MQWs, and this provides an efficient surface passivation. Reducing the surface recombination in the active region improves the carrier confinement and results in higher gain and efficiency. A peak fiber-to-fiber gain of 17 dB was obtained.

For WAPs, selective undercut etching the InGaAsP-based MQW in the amplifier region was crucial to avoid current crowding of the injection current. The sheet resistance of the p-contact layer is the source of current crowding. This is a general problem for many p-n junction devices relying on current

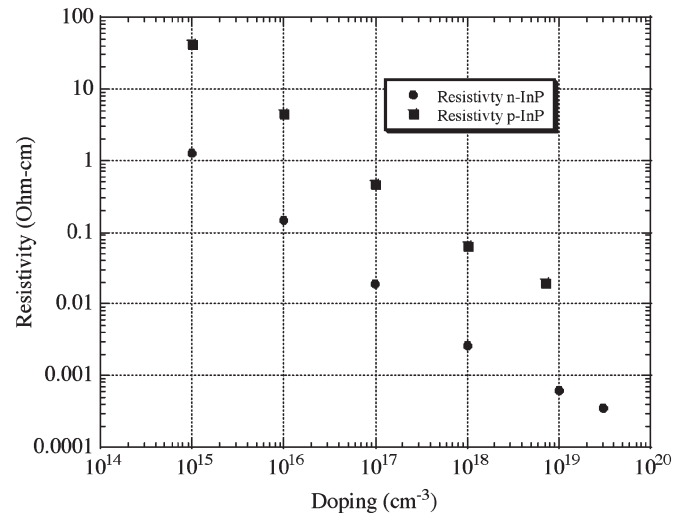


Fig. 14. Resistivity of p-InP and n-InP versus doping concentration.

injection. P-layers have higher resistivities than n-layers and therefore have higher sheet resistances and contact resistances. Upon injection from the p-metal contact, the current will not spread evenly over the junction; instead, it tends to crowd at the edge of the junction. Selective undercut etching is one way of confining the injection current to the center of the junction; other techniques include oxidation, ion implantation, and regrowth. Many previous reports can be found discussing current confinement, a review is found in [15]. Fig. 14 shows the difference in resistivities of n-InP and p-InP as functions of doping, calculated from mobility data in [22]. For a WAP, it was also shown that undercut etching InGaAs (in the detector region) reduces detector leakage current. RIE patterning of the detector causes a sidewall damage and leaves a hydrocarbon contamination, which increase detector leakage current. A short undercut etching of InGaAs in the detector region removes damaged sidewalls and contaminants (this etching needs to be very short or a very diluted  $\text{H}_2\text{SO}_4 : \text{H}_2\text{O}_2 : \text{H}_2\text{O}$  solution should be used because InGaAs etches very fast in  $\text{H}_2\text{SO}_4 : \text{H}_2\text{O}_2 : \text{H}_2\text{O}$  solutions, cf. Table I).

The results from the etch rate and selectivity measurements are summarized in Table I.  $\text{H}_2\text{SO}_4 : \text{H}_2\text{O}_2 : \text{H}_2\text{O} = 3 : 1 : 1$  solution etches InGaAs at a very high rate; therefore, even if the etch rate of InP is higher, the relative selectivity of the 3:1:1 solution is still higher than that of the 1:1:10 solution. Probably, an even higher selectivity can be obtained for the InGaAs/InP system using  $\text{H}_2\text{SO}_4 : \text{H}_2\text{O}_2 : \text{H}_2\text{O}$  solutions by varying the relative composition ratio. It is important to have a high etch selectivity; otherwise, the etching will attack the surrounding InP cladding layer. For example, undercut etching InGaAsP MQWs by 10  $\mu\text{m}$  will etch the InP cladding layers by 105 and 330 nm in the 3:1:1 and 1:1:10 solutions, respectively. For most in-plane devices such as edge-emitting lasers, this may not be a major concern since the cladding is normally thicker than 1  $\mu\text{m}$ . However, when undercut-etching devices such as VCSELs, where the InP cladding is only a couple of hundred nanometers thick, it is important to have as high a selectivity as possible.

The anisotropy in undercut etching needs to be accounted for in the device fabrication. For example, surface micromachined microelectromechanical system (MEMS) devices can be aligned along  $\langle 001 \rangle$  to avoid anisotropic undercut etching, as seen in Fig. 1(c). This freedom in alignment is not available for in-plane devices, such as lasers, that rely on cleaved edges and therefore need to be aligned in  $\langle 011 \rangle$  directions. For a circular mesa, e.g., used in vertical-cavity devices, the result is a rectangular-shaped undercut; see Fig. 1(a). This can result in unwanted effects, such as a polarization-dependent gain (PDG) in VCSOAs. In an MEMS fabrication, corner-compensating structures have been used to reduce the effects of anisotropic undercut etching. The technique is based on compensating, in the lithographic mask, for faster etching directions [23].

In this paper,  $\text{H}_2\text{SO}_4 : \text{H}_2\text{O}_2 : \text{H}_2\text{O}$  solutions were used to selectively undercut-etch InGaAs and InGaAsP MQWs. The selectivity and etch rate of  $\text{H}_2\text{SO}_4 : \text{H}_2\text{O}_2 : \text{H}_2\text{O} = 3 : 1 : 1$  and  $\text{H}_2\text{SO}_4 : \text{H}_2\text{O}_2 : \text{H}_2\text{O} = 1 : 1 : 10$  were measured, both in  $\langle 011 \rangle$  directions and in  $\langle 001 \rangle$  directions. It was seen that many etch properties are governed by the slow-etching  $\{111\}$  A planes, such as etch rate, anisotropy, and sidewall profile. More significantly, it was also shown how selective undercut etching is an effective tool in improving the performance of long-wavelength optoelectronic devices.

#### REFERENCES

- [1] A. R. Clawson, "Guide to references on III-V semiconductor chemical etching," *Mater. Sci. Eng., R*, vol. R31, no. 16, pp. 1–438, 1992.
- [2] *Properties of Lattice-Matched and Strained Indium Gallium Arsenide*, P. Battacharya, Ed. London, U.K.: INSPEC, 1993.
- [3] *Properties, Processing, Applications of Indium Phosphide*, T. P. Pearsall, Ed. London, U.K.: INSPEC, 1999.
- [4] G. A. Ferrante, J. P. Donnelly, and C. A. Armiento, "A slow selective etch for GaInAsP on InP," *J. Electrochem. Soc.*, vol. 130, no. 5, pp. 1222–1224, May 1983.
- [5] D. I. Elder and A. R. Clawson, "Determination of In<sub>0.53</sub>Ga<sub>0.47</sub>As layer thickness from etched steps," *J. Mater. Sci. Lett.*, vol. 3, no. 4, p. 340, 1984.
- [6] F. Fieldler, A. Schlachetzki, and G. Klein, "Material-selective etching of InP and an InGaAsP alloy," *J. Mater. Sci.*, vol. 17, no. 10, pp. 2911–2918, Oct. 1982.
- [7] A. Stano, "Chemical etching characteristics of InGaAs/InP and InAlAs/InP heterostructures," *J. Electrochem. Soc.*, vol. 134, no. 2, pp. 448–452, Feb. 1987.
- [8] E. S. Bjorlin, T. Kimura, and J. E. Bowers, "Carrier confined vertical-cavity semiconductor optical amplifiers for higher gain and efficiency," *IEEE J. Sel. Topics Quantum Electron.*, vol. 9, no. 5, pp. 1374–1385, Sep./Oct. 2003.
- [9] J. Piprek, D. Lasaosa, D. Pasquariello, and J. E. Bowers, "Physics of waveguide photodetectors with integrated amplification," in *Proc. SPIE Physics and Simulation Optoelectronic Devices XI, Photonics West*, San Jose, CA, 2003, vol. 4986-28, pp. 214–221.
- [10] J. Piprek, P. Abraham, and J. E. Bowers, "Cavity lengths effects on internal loss and quantum efficiency of multi-quantum-well lasers," *IEEE J. Sel. Topics Quantum Electron.*, vol. 5, no. 3, pp. 643–647, May/Jun. 1999.
- [11] S. Nakagawa, E. Hall, G. Almuneau, J. K. Kim, D. A. Buell, H. Kroemer, and L. A. Kroemer, "1.55- $\mu\text{m}$  InP-lattice-matched VCSELs with AlGaAsSb-AlAsSb DBRs," *IEEE J. Sel. Topics Quantum Electron.*, vol. 7, no. 2, pp. 224–230, Mar./Apr. 2001.
- [12] L. Tenerz, Y. Bäcklund, J. Tiren, and J. O'Connell, "Perpendicular walls fabricated in  $\langle 100 \rangle$ -oriented silicon by anisotropic," *Sens. Mater.*, vol. 1, no. 7, pp. 313–320, 1989.
- [13] S. Zhang, "Travelling-wave electroabsorption modulators," Ph.D. dissertation, Dept. Elect. Comput. Eng., Univ. California, Santa Barbara, 1999.
- [14] P. A. Rizzi, *Microwave Engineering Passive Circuits*. Englewood Cliffs, NJ: Prentice-Hall, 1987.
- [15] L. A. Coldren and S. W. Corzine, *Diode Laser and Photonic Integrated Circuits*. New York: Wiley, 1995.
- [16] S. R. Geels, B. J. Thibeault, S. W. Corzine, J. W. Scott, and L. A. Coldren, "Design and characterization of InGaAs MQW vertical-cavity surface-emitting lasers," *IEEE J. Quantum Electron.*, vol. 29, no. 12, pp. 2977–2987, Dec. 1993.
- [17] Z. Liao, J. Walpole, and D. Tsang, "Fabrication, characterization, and analysis of mass-transported GaInAsP/InP buried heterostructure lasers," *IEEE J. Quantum Electron.*, vol. QE-20, no. 8, pp. 855–865, Aug. 1984.
- [18] C. H. Cox, G. E. Betts, and L. M. Johnson, "An analytical and experimental comparison of direct and external modulation in analog fiber-optic links," *IEEE Trans. Microw. Theory Tech.*, vol. 38, no. 5, pp. 501–509, May 1990.
- [19] J. E. Bowers and C. A. Burrus, "Ultrawide-band long-wavelength p-i-n photodetectors," *J. Lightw. Technol.*, vol. LT-5, no. 10, pp. 1339–1350, Oct. 1987.
- [20] D. Lasaosa, Y.-J. Chiu, J. Piprek, and J. E. Piprek, "Modeling of traveling-wave amplification photodetector," in *Proc. SPIE Physics and Simulation Optoelectronic Devices XI, Photonics West*, San Francisco, CA, 2000, vol. 4283-64, pp. 32–37.
- [21] T. Böttner, H. Kräutle, E. Kuphal, K. Miethe, and H. L. Hartnagel, "Surface- and sidewall-damage of InP-based optoelectronic devices during reactive ion etching using  $\text{CH}_4/\text{H}_2$ ," in *Proc. Indium Phosphide and Related Materials (IPRM)*, Schwabisch-Gmund, Germany, 1996, pp. 115–118.
- [22] S. Datta, K. P. Roenker, M. M. Cahay, and W. E. Stanchina, "Implications of hole versus electron transport properties for high speed pnp heterojunction bipolar transistors," *Solid State Electron.*, vol. 43, no. 1, pp. 73–79, Jan. 1999.
- [23] P. Enoksson, "New structure for corner compensation in anisotropic KOH etching," *J. Micromech. Microeng.*, vol. 7, no. 3, pp. 141–144, 1997.

**Donato Pasquariello**, photograph and biography not available at the time of publication.

**E. Staffan Björin** (S'00–M'02), photograph and biography not available at the time of publication.

**Daniel Lasaosa**, photograph and biography not available at the time of publication.

**Yi-Jen Chiu**, photograph and biography not available at the time of publication.

**Joachim Piprek** (M'94–SM'98), photograph and biography not available at the time of publication.

**John E. Bowers** (S'78–M'81–SM'85–F'93), photograph and biography not available at the time of publication.